POLITECNICO DI TORINO
Repository ISTITUZIONALE

Electron-beam charge injection for contactless small-angle alignment in graphene/hBN heterostructures

*Original*
Electron-beam charge injection for contactless small-angle alignment in graphene/hBN heterostructures / Curreli, N., Kulmala, T.S., Sebait, R., Petrini, N., Lodi, M.B., Furrer, R., Fanti, A., Calame, M., Kriegel, I.. - In: NPJ 2D MATERIALS AND APPLICATIONS. - ISSN 2397-7132. - 10:1(2026), pp. 1-9. [10.1038/s41699-025-00658-x]

*Availability:*
This version is available at: 11583/3014871 since: 2026-08-26T06:49:52Z

*Publisher:*
Springer Nature

*Published*
DOI:10.1038/s41699-025-00658-x

*Terms of use:*

This article is made available under terms and conditions as specified in the corresponding bibliographic description in the repository

*Publisher copyright*

(Article begins on next page)

27 November 2026

npj | 2D materials and applications

Article

Published in partnership with FCT NOVA with the support of E-MRS

https://doi.org/10.1038/s41699-025-00658-x

# Electron-beam charge injection for contactless small-angle alignment in graphene/hBN heterostructures

Check for updates

Nicola Curreli[1,2,3] ✉, Tero S. Kulmala[2], Riya Sebait[2,4], Nicolò Petrini[1,3], Matteo Bruno Lodi[5], Roman Furrer[2], Alessandro Fanti[5], Michel Calame[2,6] & Ilka Kriegel[1,3]

The ability to dynamically control the relative orientation of layers in two-dimensional (2D) van der Waals (vdW) heterostructures represents a critical step toward the realization of reconfigurable nanoscale devices. Existing actuation methods often rely on mechanical contact, complex architectures, or extreme operating conditions, which limit their applicability and scalability. In this work, we present a proof-of-concept demonstration of contactless electrostatic actuation based on electron-beam-induced charge injection. By locally charging an insulating hexagonal boron nitride (hBN) flake on an electrically grounded graphene layer, we create an interfacial electric field that generates in-plane electrostatic torque and induces angular displacement. The resulting small-angle alignment of the graphene/hBN heterostructure is confirmed through in-situ scanning electron microscopy (SEM) and twist-dependent Raman spectroscopy.

The growing field of reconfigurable nano-devices has attracted significant attention due to its potential to impact various technological areas, including advanced sensors, actuators, and next-generation electronic components[1,2]. This interest originates from the distinct physical and chemical properties of materials at the nanoscale, which often differ significantly from their bulk counterparts, allowing for new functions[3–8]. The ability to manipulate and control the state of nanoscale systems through actuation mechanisms is important to fully exploit their functionality and improve the performance of nanoscale devices[1]. A technological platform that puts these actuation principles into practice is provided by nano- and micro-electromechanical systems (N/MEMS), which integrate movable mechanical structures with their driving and sensing electronics on the same chip[1]. Among the different materials investigated within N/MEMS architectures, two-dimensional (2D) van der Waals (vdW) materials have emerged as particularly promising candidates[1]. Moreover, combining distinct 2D materials into heterostructure architectures not only allows precise tailoring of the properties of each individual component, but, more importantly, also opens pathways to unique device functionalities that would otherwise be impossible[6,9–11]. Recent research has explored several actuation mechanisms for 2D materials, including piezoelectric[12,13], piezoresistive[14], opto-thermal[15,16], and electrostatic[1] approaches, which are frequently implemented within N/MEMS platforms to exert controlled forces or strain. For instance, piezoelectric actuation has been explored for monolayer hexagonal boron nitride (hBN), which exhibits piezoelectric properties due to the lack of a center of symmetry, suggesting its potential for electromechanical devices[13]. However, the piezoelectric response in ultrathin layers can be limited, and factors such as stress induced during fabrication and potential contamination can affect device performance[13]. On the other hand, opto-thermal actuation presents a contactless approach to manipulating 2D materials, typically relying on the use of lasers to induce localized heating and thermal expansion[15]. For example, micro-heaters can achieve controlled biaxial strain in 2D materials via thermal expansion[16]. Nevertheless, this method can be constrained by requirements for high-temperature processing, the risk of material degradation due to heating, and the complexity of experimental setups. Another example of actuation exploits the piezoresistive effect of suspended graphene membranes with attached silicon proof masses to realize a piezoresistive N/MEMS accelerometers[14]. While offering mechanical control, this approach can introduce stress during fabrication, potential contamination from the substrate, and complexities in device integration. In this context, electrostatic actuation, which relies on Coulombic forces, has been extensively explored as a versatile technique for manipulating N/MEMS due to its inherent potential for achieving high

[1]Department of Applied Science and Technology, Polytechnic University of Turin, Turin, Italy. [2]Transport at Nanoscale Interfaces Laboratory, EMPA, Swiss Federal Laboratories for Materials Science and Technology, Dübendorf, Switzerland. [3]Functional Nanosystems, Italian Institute of Technology, Genoa, Italy. [4]Nanotechnology at Surfaces Laboratory, EMPA, Swiss Federal Laboratories for Materials Science and Technology, Dübendorf, Switzerland. [5]Department of Electrical and Electronic Engineering, University of Cagliari, Cagliari, Italy. [6]Department of Physics and Swiss Nanoscience Institute, University of Basel, Basel, Switzerland. ✉e-mail: nicola.curreli@unica.it; nicola.curreli@polito.it

operating frequencies and its relative ease of integration into device architectures[1]. In fact, at the microscale, Coulomb forces arising from net charges or induced polarization can overcome the weak vdW interactions between layers[17]. In principle, these forces can address several mechanical degrees of freedom in stacked 2D crystals, such as out-of-plane separation, in-plane strain, and relative rotation[18]. The latter, quantified by the interlayer twist angle, controls the formation of moiré superlattices and thereby tunes a plethora of correlated electronic and optical phenomena[3,19]. Deterministic twist control is therefore a primary goal; however, achieving precise and reproducible tuning of the twist angle has proven remarkably challenging. Indeed, most electrostatic schemes reported to date induce lateral sliding or bending rather than deterministic rotation[1]. Closing this gap is a key prerequisite for truly reconfigurable 2D heterostructures. A promising route is to tailor the charge distribution so that the resulting lateral electric field exerts an electrostatic torque, rotating the adjacent layers. Several strategies have been proposed to exploit this concept. Solution-based methods use surface charges in liquid environments (e.g., through solvents, pH, or ionic screening) to assist in the assembly and alignment of 2D materials[20]. Charged 2D flakes in liquid can self-assemble with a tendency toward commensurate alignment due to electrostatic interactions overcoming random vdW attachment, although they offer limited post-deposition control[20]. Tip-based charge injection techniques provide a tool for achieving highly localized electrostatic control over 2D materials at the nanoscale[21]. A sufficiently high bias voltage between the conductive tip and the sample can inject charges into the 2D material by overcoming local energy barriers, primarily through electron tunneling across the thin insulating layer between the tip and the 2D material[22]. These techniques suffer from the significant drawback that the mechanical contact often required between the tip and the sample can introduce unwanted strain, contamination, or even physical damage to the atomically thin 2D layers.

To overcome the limitations of the aforementioned methods, this work introduces a proof-of-concept demonstration of contactless electrostatic actuation of 2D vdW heterostructures exploiting direct charge injection via an electron beam. The core mechanism of our approach can be described through a nanoscale parallel-plate capacitor model. The bottom layer of the heterostructure, consisting of graphene, is electrically grounded and serves as a stator, establishing a fixed reference potential. The top layer, composed of hBN, adheres to graphene only through vdW forces, and due to the incommensurate alignment in our system, exhibits ultralow interlayer shear strength[23]. Hence, for the in-plane rotational degree of freedom, the flake behaves as a mechanically decoupled rotor. When a focused scanning electron microscope (SEM) beam is directed onto the hBN flake, electrons accumulate on its surface, inducing a potential difference with respect to the grounded graphene. This generates an electrostatic field with both vertical and lateral components at the interface. While the vertical component drives interlayer attraction, the lateral field components are responsible for producing an in-plane torque that acts to align the hBN flake with the underlying graphene[24]. The rotational response of the system proceeds until a mechanical equilibrium is achieved, defined by the balance between electrostatic torque and the mechanically resistive torque due to vdW static friction[25]. To validate the electrostatically driven rotation, we combine in-situ SEM imaging and Raman spectroscopy as complementary non-contact diagnostics[26]. SEM imaging tracks the twist angle between the graphene and hBN layers in real time by directly resolving the angle between adjacent flakes. Raman spectroscopy, instead, detects the moiré super-lattice through twist-dependent shifts and splittings of the Raman peaks; the period of the moiré pattern extracted from these spectral features yields an independent quantitative estimate of the twist angle[26]. Agreement between the two measurements provides a robust cross-check of the contact-free actuation.

## Results

### Device architecture and electrostatic actuation scheme

To experimentally demonstrate electron-beam-driven twist control, we carried out a series of systematic experiments on graphene/hBN heterostructures, where twist modulation was induced by electron beam exposure. The experimental setup consisted of a graphene stator, electrically grounded using an Imina Technologies nanoprobing platform, and a hexagonal boron nitride rotor. A thin gold pad was patterned on the hBN flake to serve as a charge-collection electrode, providing an equipotential surface for the accumulation of electrons delivered by the SEM beam, operated under controlled parameters (see Methods for details).

Figure 1 summarizes both the physical layout and the electrostatic operation principle. The final device layout is shown in Fig. 1a, which presents a representative SEM image of the graphene/hBN stack with the etched stator geometry (red dashed lines). This specific geometry was chosen to maximise the graphene area while maintaining electrical isolation between the individually biased pads, and at the same time to ensure that the hBN flake lies entirely on graphene, avoiding any contact with the underlying $Si/SiO_2$ substrate, thus preventing pinning or strain.

A schematic illustration of the actuation mechanism is provided in Fig. 1b, highlighting how local charge injection via electron beam leads to the generation of electrostatic torque driving the rotation of the hBN rotor. Two opposite graphene pads of the stator are biased at $\pm V_{bias}$ (<1 V) while the remaining pads are grounded, establishing a lateral potential gradient across the interface. The injected charge polarizes in response to $V_{bias}$, giving rise to an in-plane electrostatic field $\mathbf{E}_{\parallel}$ that exerts a torque on the hBN rotor and drives it towards the equilibrium twist angle controlled by the bias polarity. The graphene/hBN heterostructures were fabricated via established dry-transfer techniques onto $Si/SiO_2$ substrates. The fabrication of the heterostructures followed a multi-step approach to ensure precise patterning and stacking of the 2D materials (see Supplementary Information and Supplementary Fig. S1). Monolayer graphene was synthesized on a Cu foil substrate via chemical vapor deposition (CVD) and then transferred onto a $Si/SiO_2$ substrate (extended details are reported in Methods and Supplementary Information). A square-shaped geometry (see Fig. 1) was adopted for the graphene stator, and the CVD graphene was patterned using a combination of electron beam lithography (EBL) and reactive ion etching (RIE). Identical patterning was carried out on three separate $Si/SiO_2$ chips, each hosting a continuous monolayer graphene film. On every chip, 64 square graphene regions ($50 \times 50\ \mu m^2$) were defined, yielding a total of 192 graphene stators. From these, only the highest-quality graphene regions, free of defects such as tears, multilayer inclusions, polymer residues, or irregular etching profiles, were selected for heterostructure assembly. Subsequently, hBN flakes (~30 nm thick, see Supplementary information for details) were exfoliated and transferred onto the selected graphene regions to implement graphene/hBN heterostructures, and gold electrodes were defined to provide independent electrical access. During transfer and electrode fabrication, several heterostructures were lost due to mechanical failure or processing issues. Ultimately, six stacks exhibited twist dynamics under SEM irradiation and were analyzed in detail (extended data in Supplementary Figs. S7–S12). The SEM was equipped with a nanoprobing system to enable both charge injection and real-time observation of interfacial dynamics within the graphene/hBN heterostructures. The electron beam parameters were optimized to deliver controlled energy input while minimizing the risk of beam-induced damage. Specifically, the accelerating voltage was set to 5 keV to restrict the electron penetration depth and reduce the total dose imparted to the system. The beam was defined by a 20 $\mu m$ aperture. Beam scanning was performed over a $50 \times 50\ \mu m^2$ area with a dwell time corresponding to a scan rate of ~1 s per frame, and the beam current was maintained below 100 pA. From an energy-balance estimation, the current and voltage applied yield an energy density of $\sim 10^2 - 10^3\ Jm^{-2}$ per scan, corresponding to a dose of $2 - 4\ \mu C\ cm^{-2}$ (see Supplementary Note 2 for the detailed energy dose estimation). Under these conditions, we did not observe evidence of beam-induced lattice damage, as confirmed by Raman measurements before and after exposure (see Supplementary Note 4). Moreover, although the doses that cause damage are material dependent, the energy density applied in our experiments is orders of magnitude lower than values reported to induce significant morphological modifications in other 2D heterostructures, e.g., $Bi_2Se_3/MoS_2$ ($3 \times 10^6\ Jm^{-2}$ [24]). This supports that the damage threshold was not reached in our heterostructures; however, cross-material comparisons

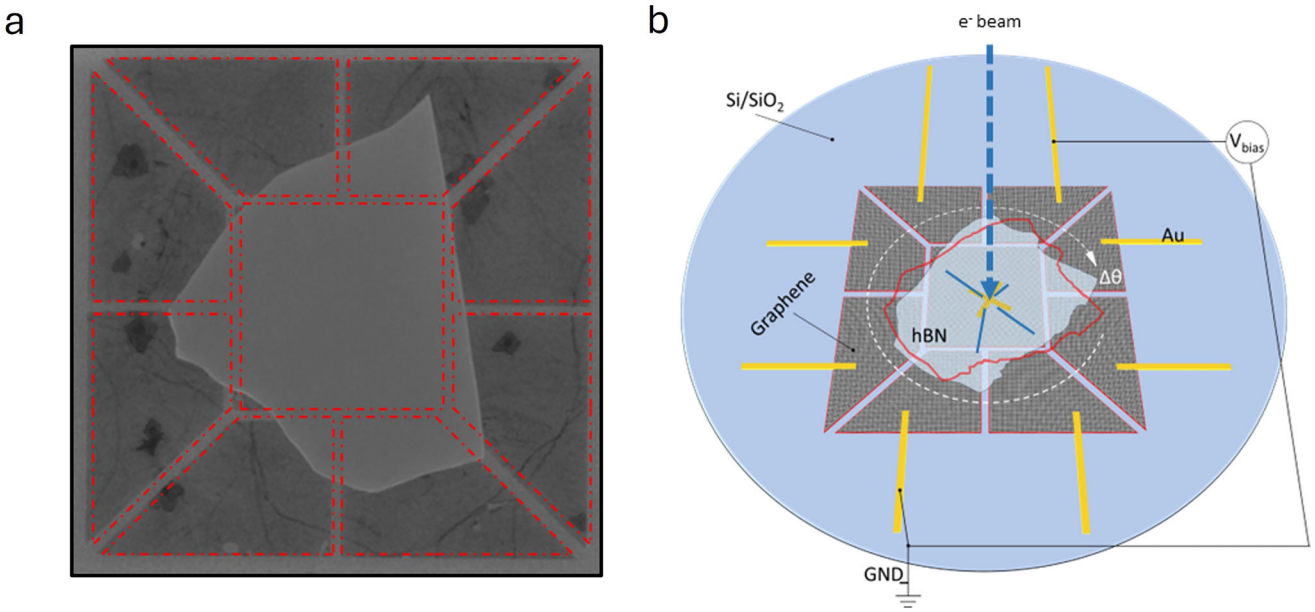


**Fig. 1 | a** Scanning electron micrograph of a representative graphene/hBN heterostructure. The bottom graphene layer (stator) is patterned into a square geometry. A mechanically decoupled hBN flake (rotor) is placed atop the patterned graphene (stator). The red dashed lines highlight the etched geometry of the stator. **b** Conceptual representation of the device operation under electron beam irradiation. A focused electron beam ($e^-$ beam) locally charges the hBN layer, inducing a potential difference with respect to the grounded graphene. The resulting electrostatic field at the interface comprises vertical and lateral components. The lateral field exerts an in-plane torque on the hBN rotor (curved white arrow), starting rotational motion toward a new equilibrium twist angle.

should be interpreted with caution. A fundamental aspect of the experimental design was the implementation of a well-defined electrostatic boundary condition through the electrical grounding of the graphene layer, which served as the static electrode (stator) of the heterostructure. The ground connection established a reference potential for generating a stable electric field between the graphene and the hBN layer. In the absence of this grounding condition, charge accumulation on both layers would render the capacitive interaction uncontrollable. Under electron beam irradiation, the hBN layer acted as a mechanically decoupled rotor tuned via charge injection. The actuation mechanism, based on lateral electrostatic torque generated by asymmetric charge distribution, is depicted in Fig. 1b.

### Electron-beam-induced twist probed by in situ Scanning Electron Microscopy

Under the abovementioned conditions, SEM imaging revealed clear signs of twist modulation in our graphene/hBN stacks. To systematically investigate the effect of electron-beam-induced actuation on interlayer twist, we tested the selected graphene/hBN heterostructures under conditions designed to favor either clockwise (CW) or counterclockwise (CCW) rotation. Images acquired before and after the electrostatically induced rotation showed interlayer motion progressing toward the grounded graphene layer (the stator), consistent with electrostatically driven torque. In representative samples S1 and S2, shown in Fig. 2 and Fig. 3, respectively, a clear angular displacement of the hBN flake relative to the underlying graphene is observed.

**Sample S1**. Specifically, in Sample S1, the pre- and post-rotation configurations are shown in Fig. 2a and b, respectively (see Supplementary Fig. S7 for additional characterization of Sample S1). The corresponding twist angle is quantitatively extracted in Fig. 2c using a dedicated Python-based image registration procedure: the two SEM images are aligned based on a central region of interest centered on the gold cross atop the hBN flake, and a brute-force rigid rotation is applied to the post-rotation frame. The angle that minimizes the pixel-wise mean squared error between the two frames is identified as the actual twist, yielding a counterclockwise rotation of approximately 3° (extended details are reported in Methods and Supplementary Information). Figure 2f provides a zoomed overlay of the aligned images. This demonstrates that even a relatively low-dose electron injection, combined with a grounded graphene stator, can generate sufficient electrostatic torque to overcome interlayer friction, thus driving the hBN rotor into a new angular configuration. Given its wide bandgap (~6 eV[27]) and low intrinsic conductivity[28], hBN promotes spatially localized charge accumulation, enhanced by the limited out-of-plane transport in hBN, allowing the buildup of a quasi-static negative charge distribution. This non-uniform surface potential, in the presence of the grounded graphene stator beneath, leads to the formation of an effective electric field with both planar and perpendicular components across the heterostructure. As a result, the electron beam irradiation leads to an electrostatic force that can overcome static friction at the interface, allowing the hBN layer to rotate into an alignment that minimizes the overall system energy. The electric field exerts an electrostatic torque that rotates the hBN layer in-plane, modulating the twist angle of the graphene/hBN superlattice until the torque is balanced by interlayer vdW friction, at which point a new equilibrium is reached[24,25]. In this way, the electron beam acts as a remote control for manipulating 2D interfaces. In addition, although SEM imaging allowed us to clearly track the incremental rotation of the hBN rotor relative to the graphene stator ($\Delta\theta$), it did not provide direct access to the crystallographic twist angle ($\theta$) that defines the moiré superlattice between the two layers. This is primarily due to the lack of crystallographic reference for the individual layers before to beam exposure. This limitation prevented direct measurement of the moiré angle. However, indirect estimation of the moiré periodicity was achieved via spatially resolved Raman spectroscopy, by exploiting frequency shifts and peak broadening in the graphene 2D modes. In fact, these spectroscopic signatures are sensitive to the presence of moiré-induced modulation of the phonon dispersion and allowed us to estimate the moiré wavelength, and hence infer a range of possible twist angles, even in the absence of direct lattice imaging. Hence, to complement and further validate the results obtained from electron-beam-induced twist experiments, we performed Raman spectroscopy maps comparing two distinct regions of the sample: one consisting of monolayer graphene on the substrate, and another where the same graphene layer was covered by an hBN flake, forming a graphene/hBN heterostructure. In graphene/hBN

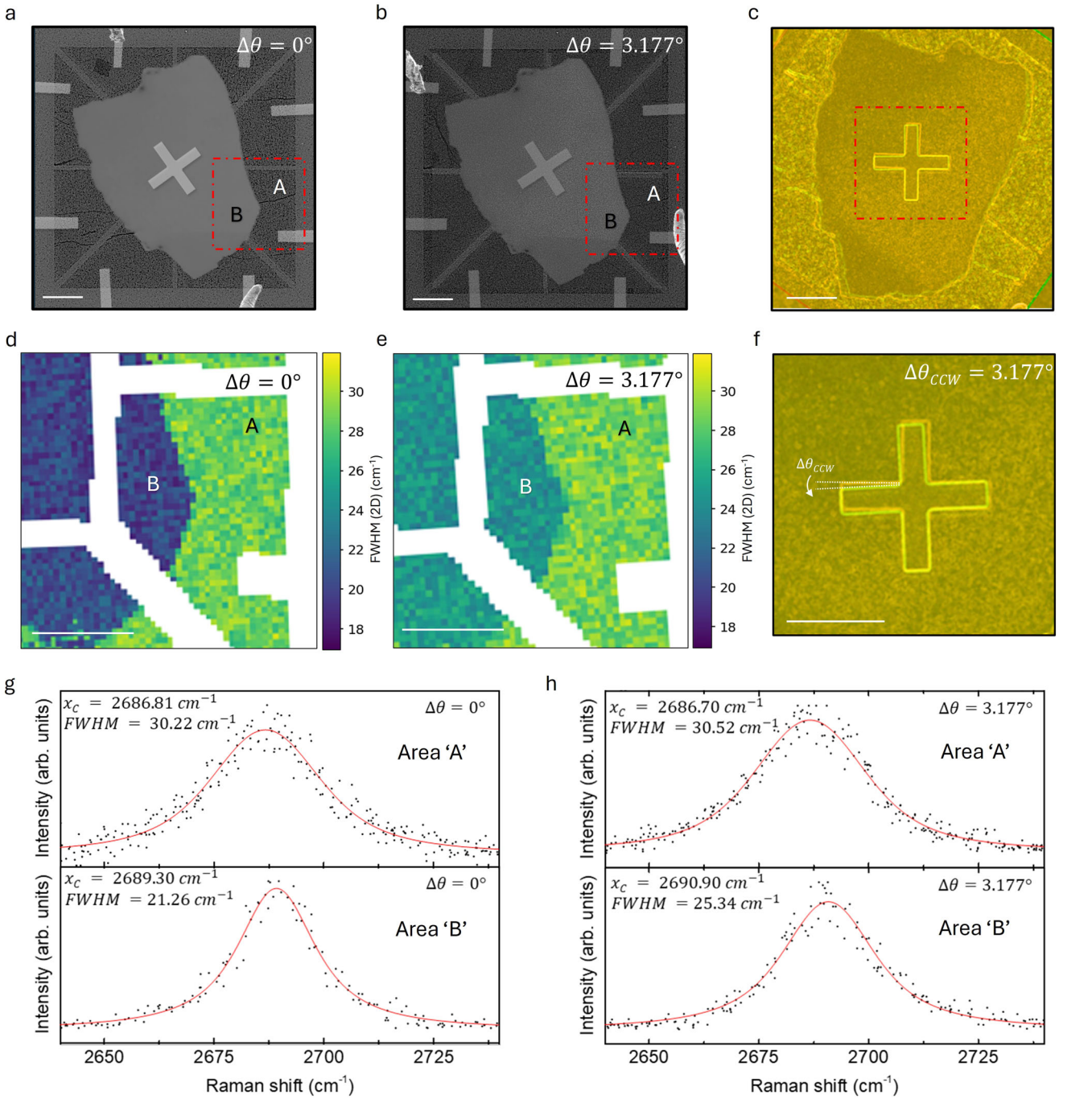


**Fig. 2 | a** Scanning electron microscopy image of Sample S1 acquired *before* electron-beam exposure; the hBN flake rests on patterned graphene pads and the red dashed rectangle marks the area analysed by Raman mapping. **b** Scanning electron microscopy image of the same region *after* electron injection, showing a counter-clockwise rotation of the flake. **c** Overlay of images **a** and **b** reveals a net twist of $\Delta\theta \approx 3.18°$. **d** Map of the full width at half maximum (FWHM) of the graphene 2D Raman band recorded *before* actuation. **e** Corresponding FWHM map *after* actuation; regions A (bare graphene) and B (graphene covered by hBN) are visible in both maps. **f** Enlarged view from **c** highlighting the measured rotation. **g** Representative Raman spectra extracted from **d**. **h** Corresponding spectra from **e**. Scale bar: 10 $\mu$m (applies to all panels).

heterostructures, the moiré pattern generated by lattice mismatch or a relative rotation angle $\theta$ induces a long-wavelength periodic potential. The associated moiré wavelength $\lambda_M$ modulates the electronic structure and introduces inhomogeneous strain in graphene, which is reflected in the Raman response through broadening and asymmetry of the 2D peak. These spectral features have been correlated with both $\lambda_M$ and $\theta$[26,29–31]. Notably, Eckmann et al.[26] reported a linear relationship between the FWHM of the 2D peak and $\lambda_M$ in monolayer graphene on hBN. Specifically, the FWHM of the 2D peak remains nearly constant at about 21 $cm^{-1}$ for $\theta > 2°$, while for $\theta < 2°$ a pronounced broadening occurs, scaling approximately linearly with $\lambda_M$. This broadening is attributed to an inhomogeneous strain distribution with the same periodicity as the moiré potential (see Supplementary Note 3 for further details). Raman spectroscopy can thus serve as a 'fingerprint' for the formation and characteristics of moiré patterns in graphene/hBN, enabling the rapid and non-destructive identification of aligned or misaligned structures. According to these studies, a broadening of the 2D peak is expected in regions where a moiré superlattice forms due to enhanced interlayer

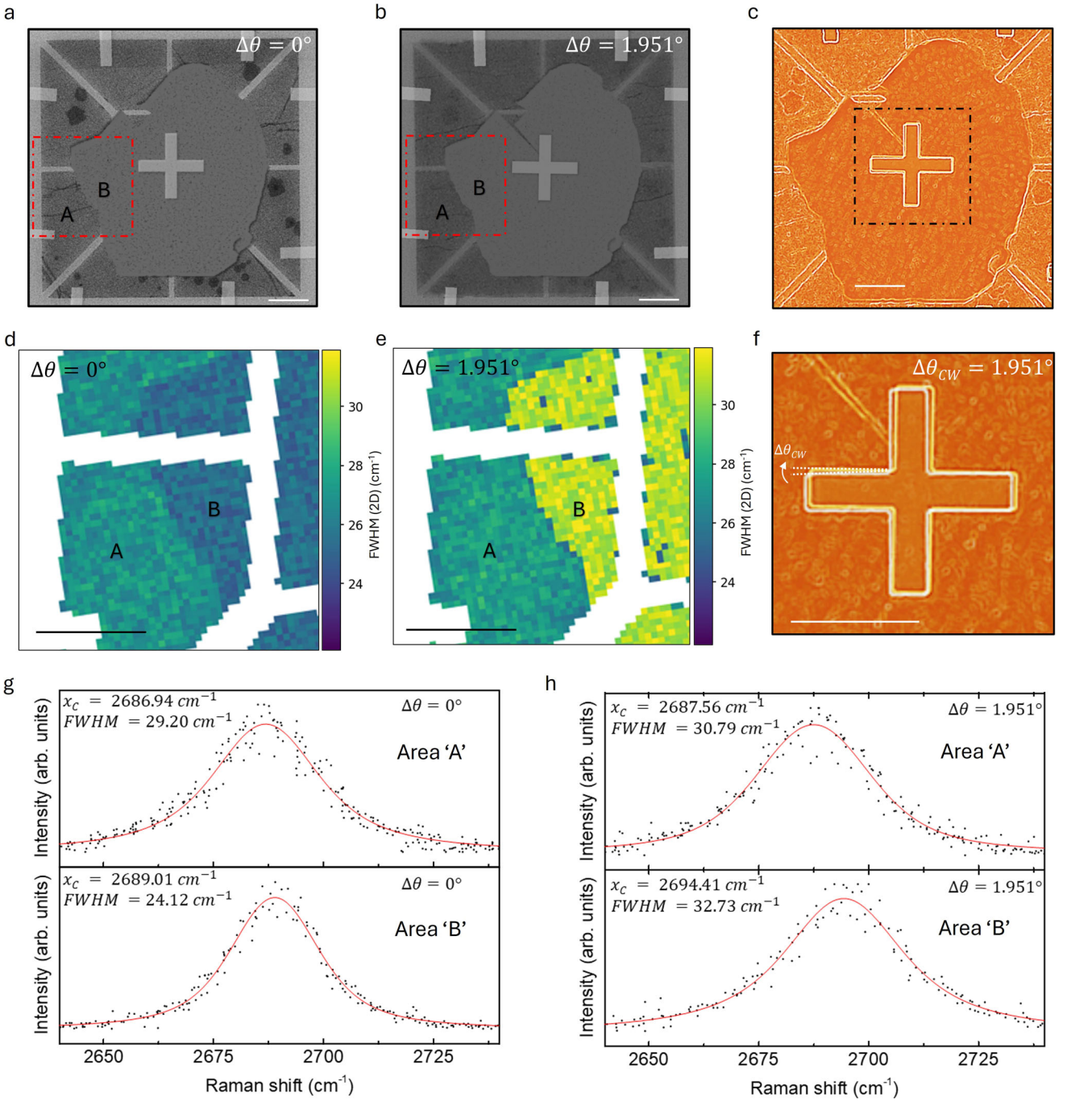


**Fig. 3 | a** Scanning electron microscopy image of Sample S2 acquired *before* electron-beam exposure; the hBN flake rests on patterned graphene pads and the red dashed rectangle marks the area analysed by Raman mapping. **b** Scanning electron microscopy image of the same region *after* electron injection, showing a clockwise rotation of the flake. **c** Overlay of images **a** and **b** reveals a net twist of $\Delta\theta \approx 1.95°$. **d** Map of the full width at half maximum (FWHM) of the graphene 2D Raman band recorded *before* actuation. **e** Corresponding FWHM map *after* actuation; regions A (bare graphene) and B (graphene covered by hBN) are visible in both maps. **f** Enlarged view from **c** highlighting the measured rotation. **g** Representative Raman spectra extracted from **d**. **h** Corresponding spectra from **e**. Scale bar: 10 $\mu$m (applies to all panels).

coupling and periodic strain. To assess the structural changes induced by this actuation mechanism, we performed spatially resolved Raman spectroscopy on the six samples before and after rotation.

First, focusing on representative sample S1, Fig. 2d and e compare the FWHM maps of the 2D Raman peak before and after electrostatic actuation, respectively. Two distinct regions are clearly visible: a graphene-only area (denoted as 'Area A') and a region where graphene is covered by the hBN flake (denoted as 'Area B'). In the graphene-only region, the FWHM remains uniform and does not exhibit significant variation after actuation. In contrast, the overlap region displays a homogeneous increase in FWHM following the rotation. This spatial modulation in the overlapping region of the heterostructure suggests a selective change in the vibrational response induced by the twist only where the two layers are in contact. These observations are corroborated by the representative Raman spectra shown in Fig. 2g and 2h. Each representative spectrum was baseline-corrected; the 2D-band intensity was normalized to the G-band intensity; all spectra belonging to the same region (pre-rotation Area A and Area B, post-rotation Area A and Area B) were then averaged and fitted with a Voigt profile to

extract the peak center position ($x_C$) and FWHM (full details in Methods). In Area A, the fit resulted in $x_C = 2686.81 \pm 0.23$ cm$^{-1}$ and FWHM = 30.22 ± 0.59 cm$^{-1}$ before rotation. After actuation, $x_C$ was found to be 2686.70 ± 0.14 cm$^{-1}$, with a corresponding FWHM of 30.52 ± 0.47 cm$^{-1}$, indicating no appreciable variation relative to the pre-actuation state. In fact, these variations fall within the experimental uncertainty and were not found to be statistically significant (t = 2.45, $p = 0.135$ for FWHM; t = 2.12, $p = 0.170$ for $x_C$), indicating that the graphene lattice outside the heterostructure region was unaffected by the induced torque (more details in Supplementary Information). On the other hand, in the graphene/hBN overlap region, the Raman response changes significantly. Before electrostatic actuation, $x_C = 2689.30 \pm 0.24$ cm$^{-1}$ with a FWHM of 21.26 ± 0.66 cm$^{-1}$. After the hBN flake underwent a CCW rotation of approximately 3°, $x_C$ shifts to 2690.90 ± 0.22 cm$^{-1}$ and broadens to 25.34 ± 0.63 cm$^{-1}$. In this case, both the shift in $x_C$ and the increase in FWHM are statistically significant (t = 19.24, $p = 0.0042$ for position; t = 10.06, $p = 0.0185$ for FWHM), confirming a twist-induced perturbation of the graphene phonon structure due to enhanced interlayer coupling. The observed FWHM broadening is consistent with the formation of a moiré superlattice, arising from a small-angle rotation between the graphene and hBN lattices.

Using the empirical relation[26]:

$$\mathrm{FWHM}\,(2D) \simeq 5 + 2.6\lambda_M \quad (1)$$

(with $\lambda_M$ in nm), the post-actuation FWHM of ~25.3 cm$^{-1}$ corresponds to a moiré wavelength of approximately 7.8 nm, consistent with a twist angle $\theta < 2°$ (see Supplementary Information for details). Conversely, the pre-actuation FWHM of ~21.3 cm$^{-1}$ suggests $\theta > 2°$, thus in line with $\Delta\theta \sim 3°$ inferred from SEM analysis. These estimates support the conclusion that the system transitions into a configuration with enhanced interlayer coupling following the electrostatic rotation. It should be noted that the correlation between the 2D-band FWHM and the moiré wavelength, as reported by ref. 26, is valid only in the small-angle regime ($\theta \lesssim 2°$). The FWHM(2D) is therefore used qualitatively to identify near-aligned regions and to corroborate the SEM-derived twist variation, while $\Delta\theta$ is obtained from SEM image registration.

**Sample S2**. Similarly, for Sample S2, SEM imaging shows a CW rotation of the hBN flake by ~2°, as shown in Fig. 3a and 3b (see Supplementary Fig. S8 for additional characterization of Sample S2). The relative displacement of the flake with respect to the underlying graphene layer is clearly visible in Fig. 3c and 3f, and the presence of a crack near the center provides a reference marker for tracking the angular shift, further confirming the occurrence of interlayer motion following electrostatic actuation. The corresponding FWHM maps of the 2D Raman peak, shown in Fig. 3d and 3e, reveal the evolution across the heterostructure before and after rotation. As in Sample S1, two regions can be distinguished: the bare graphene area (Area A) and the graphene/hBN overlap (Area B). Again, in the graphene-only region, the FWHM remains uniform and shows no appreciable change after actuation. In contrast, a clear increase in FWHM is observed in the overlap region. Notably, an inversion in the relative FWHM values occurs: while in the pre-actuation condition the FWHM was larger in the bare graphene compared to the overlap region, after actuation, the FWHM becomes higher in the overlap area. This inversion indicates a localized modification of the vibrational properties induced by interlayer rotation. This behavior is confirmed by the representative Raman spectra extracted from both regions, shown in Fig. 3g and h. In Area A, $x_C = 2686.94 \pm 0.24$ cm$^{-1}$ with a FWHM of 29.20 ± 0.69 cm$^{-1}$ before actuation, and $x_C = 2687.56 \pm 0.16$ cm$^{-1}$ with a FWHM of 31.29 ± 0.47 cm$^{-1}$ after actuation. The variations in both peak position and linewidth are limited, and statistical analysis confirms that these differences are not significant ($p = 0.784$ for FWHM; $p = 0.974$ for peak position), indicating that the graphene lattice in the uncovered region remains unaffected by the electrostatic rotation. In contrast, the graphene/hBN overlap region shows more substantial spectral modifications. The 2D peak shifts from 2689.01 ± 0.16 cm$^{-1}$ to 2694.41 ± 0.23 cm$^{-1}$, and the FWHM increases from 24.12 ± 0.44 cm$^{-1}$ to 32.73 ± 0.74 cm$^{-1}$ following the $\Delta\theta \sim 2°$ rotation. These changes are statistically significant ($t = 4.86$, $p = 0.040$ for peak position; $t = 4.48$, $p = 0.046$ for FWHM), confirming a twist-induced modulation of the graphene phonon spectrum due to interlayer reconfiguration. The observed FWHM broadening and peak shift in the overlap region are consistent with the formation of a quasi-aligned moiré superlattice, which introduces periodic strain within the graphene layer. This interpretation is further supported by the appearance of asymmetry in the 2D peak lineshape after actuation, and by the absence of spectral changes in the uncovered graphene region. Using the empirical relation (1), the measured FWHM values of 24.12 cm$^{-1}$ and 32.73 cm$^{-1}$ correspond to moiré wavelengths of approximately 7.35 nm and 10.67 nm, respectively. The increase in $\lambda_M$ after actuation reflects a reduction in the twist angle $\theta$, consistent with the transition toward a more aligned stacking configuration. While Raman spectroscopy provides access to the absolute twist angle $\theta$, the SEM analysis yields only the relative angular displacement $\Delta\theta$ between the pre- and post-actuation states. Since each measured moiré wavelength $\lambda_M$ corresponds to a specific twist angle $\theta$, determining the sign and magnitude of a change $\Delta\theta$ requires adopting a consistent angular convention or relying on additional experimental indicators. Raman spectroscopy yields a twist change of $\Delta\theta \sim 2.42°$, in good agreement with the ~ 2° CW rotation estimated from SEM images using the image-based analysis described previously, considering the combined uncertainties of both methods (see Supplementary Note 3 for further details).

### Twist-angle stability across devices

While the experiments demonstrated the feasibility of inducing twist in vdW heterostructures through localized electrostatic torque, important limitations in precision, reversibility, and angular control were observed. First, the electrostatically induced torque becomes insufficient to overcome interlayer friction and adhesion when the system moves beyond the small-angle regime. Moreover, although the structure can be actively driven out of its initial configuration, the induced motion is irreversible: once a new angular state is reached, it remains pinned and cannot be restored to the initial orientation by further electron-beam actuation. Under repeated exposures, no additional reconfiguration was detected (see Supplementary Note 4 for further details). In particular, the direction of rotation is consistently governed by the in-plane component of the electric field arising from the applied potential difference, whereas the final angular configuration is set by the energy landscape encountered during rotation, namely by the rotor's interaction with the moiré potential landscape. We attribute this behavior to a transition from a metastable to a stable state, in which the rotor becomes trapped in the first accessible local energy minimum. In addition, the process was non-deterministic, as the final twist angle could not be predictably controlled by adjusting $V_{\mathrm{bias}}$ alone. This behavior may result from the interplay between the applied bias and experimental parameters that coevolve during irradiation, including, for example, the local charge distribution induced by the SEM electron beam, the presence of metal contacts, local variations in hBN thickness and permittivity that modulate the electric field, edge orientation, adhesion and strain, and trapped charges or adsorbates at the interfaces. Since the electrostatic torque evolves dynamically under these coupled effects, the system likely settles into the first energetically accessible configuration rather than a bias-defined target angle. These observations are consistent with theoretical and experimental studies, which have shown that rotated 2D material heterostructures exhibit complex energy landscapes arising from the interplay of interlayer vdW forces and moiré superlattice formation[32–34]. These landscapes are characterized by a discrete set of preferred twist angles, often corresponding to commensurate or quasi-commensurate stacking configurations, toward which the system can spontaneously relax. Once such a configuration is reached, the interlayer friction and elastic relaxation combine to stabilize the system in a stable state, which cannot be reconfigured without overcoming substantial

energy barriers[34]. In our samples, this phenomenon manifests as a spontaneous locking of the hBN layer at a finite rotation angle following charge-induced actuation. Overall, while at the present stage this technique is still subject to the described limitations, at the same time it highlights that charge-injection-induced rotation is already capable of overcoming interlayer friction and stabilizing new angular configurations, laying the groundwork for future developments toward more precise and reversible control.

## Discussion

In this work, we have shown that electron-beam-induced charge injection can generate lateral electrostatic fields strong enough to overcome the static friction at the interface between monolayer graphene and a mechanically decoupled hBN flake, resulting in partially controlled in-plane rotation. The effect was observed across six devices, with angular displacements of a few degrees. Three rotated clockwise and three counterclockwise, in line with the bias configuration used during actuation and consistent with an electrostatic origin. This electrostatic actuation scheme offers a scalable route for post-fabrication fine-tuning of moiré devices and for studying charge-induced interlayer torque phenomena. SEM images allowed us to track the angular motion while spatially resolved Raman spectroscopy provided an independent signature of interlayer reconfiguration through measurable broadening of the graphene 2D band. Actuation is contactless on the rotor, with the SEM serving as an external trigger for a pre-assembled rotor-stator stack. In addition, the proposed approach does not require integrating micro-electromechanical components. Electron-beam charge injection enables reliable, contactless alignment control in graphene/hBN heterostructures within the small-angle regime. The observed motion is, however, irreversible under current conditions. Once the flake settles into a new angular configuration, it remains pinned, likely due to energy minima in the moiré potential landscape. Looking ahead, we anticipate that this actuation principle can be implemented in a fully on-chip, integrated architecture, by adding a top contact connected to the stator via vertical feedthroughs, enabling the generation of lateral electric fields by applying a small bias directly across the structure. Additional improvements may include segmenting the stator into multiple addressable regions to tune the torque distribution and achieve finer angular control. Extending the concept to other materials, such as 2D transition metal dichalcogenides, will broaden the range of twist-sensitive physical responses that could be accessed and dynamically tuned. In summary, this work demonstrates that internal electrostatic forces can be harnessed to induce rotational motion in 2D heterostructures. Integrating this concept into a fully lithographic platform using via-hole contacts may offer a practical route toward reconfigurable devices where the twist degree of freedom becomes a functional parameter, enabling new approaches in optoelectronics, photonics, and quantum materials.

## Methods

### Sample preparation

CVD graphene was synthesized on commercial copper foil (25 $\mu$m thick, Alfa Aesar, 99.8% purity, purchased in 2022). To promote the formation of large copper grains, the foils were pre-annealed in a three-zone tube furnace (HZS, Carbolite) in two steps: first at 400 °C for 2-4 h, then at 1060 °C for 2-12 h under an $H_2$/Ar mixture (20 sccm $H_2$, 200 sccm Ar) at ~ 1 mbar. Following annealing, the foils were electropolished in 70% $H_3PO_4$ at 2.2 V until the current decreased to less than half of its initial value. The copper foils were then cleaned by sequential sonication in acetone (5 min), rinsing with isopropanol (IPA), immersion in $HNO_3$ (30 min), two rounds of DI-water sonication (1 min each), immersion in ethanol (1 min), and drying with $N_2$ gas. The cleaned foils were reloaded into the same quartz tube furnace, and the temperature was set to 1000 °C under a $H_2$/Ar mixture (20 sccm $H_2$, 200 sccm Ar) at ~ 1 mbar. After 75 min, graphene growth was initiated using $CH_4$ (0.04 sccm) for 35 min at 1000 °C and 110 mbar, subsequently cooled by opening the temperature shielding. Subsequently, a 50K PMMA resist (Allresist) was spin-coated onto the graphene/copper surface at 3000 rpm for 40 s. Reactive ion etching (Oxford PlasmaPro NPG 80, 30 sccm oxygen and 15 sccm argon, 25 W RF power for 30 s) was employed to remove graphene from the backside of the copper foil[35]. The graphene transfer process was carried out as reported in Supplementary S1b of[36]. A PMMA-protected graphene sheet on a copper substrate is placed on the surface of a Transene copper etchant (CE-100) for 60 min. Once the etching is completed, graphene is transferred with a spoon in sequence to two deionized water baths and a 1:3 solution of HCl 37%: deionized water to remove traces of copper etchant, and finally to a third deionized water bath. From this last water bath, the graphene sheet is transferred on the $Si/SiO_2$ substrate by fishing, and let dry inside an upside-down beaker to avoid surface contamination, with an inclination of 30° - 45°, for 1.5 hours. Afterwards, the $Si/SiO_2$/graphene sample is annealed first at 80 °C for 30 min in air, and then at 80 °C in vacuum over-night to remove water residues and increase the adhesion of graphene. The protective PMMA layer on top of graphene is then removed by first placing the samples in acetone for 10 minutes, and then boiling acetone at 54 °C for 1 h. The sample is finally rinsed in isopropyl alcohol and blown dried with a nitrogen gun.

Hexagonal boron nitride flakes with a nominal thickness of approximately 30 nm (see Supplementary Note 4 for further details) were obtained via mechanical exfoliation from bulk hBN crystals (HQ Graphene)[37,38]. The exfoliation process was performed using a standard adhesive tape-based method (Scotch Magic Tape 810, 3M). A fresh surface of the bulk crystal was first brought into contact with the adhesive side of a tape and subjected to repeated folding and unfolding cycles to progressively thin down the material. The tape carrying the exfoliated flakes was then gently pressed onto a clean $SiO_2/Si$ substrate (with a 285 nm thick thermally grown $SiO_2$ layer) under ambient conditions. After ensuring conformal contact, the tape was slowly peeled off, leaving behind a distribution of hBN flakes on the substrate surface. Optical microscopy was used to locate candidate flakes, and the thickness was estimated based on optical contrast and subsequently confirmed by atomic force microscopy in tapping mode. All substrates were cleaned in acetone and isopropanol and dried under nitrogen flow prior to exfoliation to minimize contamination and improve flake adhesion. A transparent elastomer stamp was prepared by drop-casting poly(-propylene carbonate) (PPC, Sigma-Aldrich, CAS 25511-85-7) onto a PDMS layer supported by a clean glass slide. The assembly was briefly heated to ~ 60 °C to ensure uniform spreading and adhesion of the PPC to the PDMS surface. Using a micromanipulator-based transfer stage (HQ Graphene), the PPC/PDMS stamp was aligned and brought into contact with the selected hBN flake at a substrate temperature of ~ 40 °C. The flake adhered to the PPC layer and was lifted from the substrate. The hBN flake was aligned over the target graphene and brought into contact using the same transfer setup. Heating the stage to ~ 90 °C promoted adhesion between hBN and graphene, after which the stamp was retracted, leaving the hBN in place. The remaining PPC residue was removed by immersion in chloroform followed by isopropanol, and the sample was dried under nitrogen flow[39].

CVD graphene was patterned by first spin-coating a 60-nm-thick layer of PMMA 50k (AR-P 632.06, Allresist GmbH) on it and baking the sample for 5 min at 180 °C on a hot plate followed by spin-coating of a 60-nm-thick layer of PMMA 950 k (AR-P 672.02, Allresist GmbH) and a 5 min bake at 180 °C on a hot plate. Electron beam lithography was carried out with a Vistec EBPG 5200+ system, and the samples were developed by rinsing them in 1:4 MIBK:IPA solution for 60 s followed by a brief rinse in pure IPA and drying with a nitrogen gun. The exposed graphene was etched with an Oxford PlasmaPro NPG 80 system using a mixture of oxygen (30 sccm) and argon (15 sccm), RF power of 25 W, and an etching time of 8 s. The PMMA was removed by soaking overnight in N-Methyl-2-pyrrolidone (NMP). For patterning the metal electrodes, a 320-nm-thick layer of PMMA/MA 33% (AR-P 617.06, Allresist GmbH) was spin-coated and baked for 5 min at

180 °C on a hot plate followed by spin-coating of an 87-nm-thick layer of PMMA 950 k (AR-P 672.02, Allresist GmbH) and a 5 min bake at 180 °C on a hot plate. Electron beam lithography patterning and developing were then carried out as in the case of graphene etching, and 5 nm titanium and 60 nm gold were evaporated on the sample using an Evatec BAK501 LL electron beam evaporator. Finally, a lift-off of the metal was carried out in DMSO heated to 80 °C, followed by a rinse in IPA and drying of the samples with a nitrogen gun.

### Atomic Force Microscopy

AFM imaging and thickness metrology were performed on a Park Systems XE-100 (Park Systems, Korea) in intermittent-contact (tapping) mode using PPP-NCHR silicon cantilevers (NanoWorld AG, Neuchâtel, Switzerland; nominal tip radius <10 nm; resonance ~330 kHz). Candidate hBN flakes were pre-selected by optical contrast on 285 nm $SiO_2$/Si substrates. Images (512 × 512 pixels) were acquired at a scan rate of 0.2 Hz, keeping the setpoint >65% of the free oscillation amplitude. Height profiles were extracted across flake edges to determine step height relative to the substrate; the samples were analyzed with Gwyddion 2.53. Exfoliated hBN thicknesses typically ranged 29–31 nm (see Supplementary Note 4 for further details).

### Scanning Electron Microscopy

SEM imaging was performed on a JEOL JSM-6490LA (JSM-6500 series; JEOL Ltd., Japan) using a secondary-electron detector with an accelerating voltage of 5 kV and beam currents below 100 pA using a fixed 20 $\mu$m condenser aperture. No hardware drift-compensation routine was engaged; instead, image stability was ensured by using single-frame acquisitions of ~1 s per 50 × 50 $\mu m^2$ area, which minimizes drift without additional exposure or averaging. No measurable drift or distortion was detected within the acquired images, as verified through the registration analysis described below.

For actuation, the SEM was operated at 5 kV to minimize beam damage. Beam parameters were calibrated to deliver a sufficient electron dose to induce rotation while preserving crystal quality. Full details and dose estimates are reported in the Discussion and Supplementary Information.

In-situ electrical probing was carried out inside the SEM using an Imina Technologies micromanipulation platform (Plan-les-Ouates, Switzerland) equipped with tungsten microprobes. A Keithley 2612 SourceMeter (Keithley Instruments, Cleveland, OH, USA) provided the ground reference and, when required, an applied bias to the contacted pads.

### Raman Spectroscopy

Measurements were performed on a Renishaw inVia micro-Raman system (Renishaw plc, Wotton-under-Edge, UK; 532 nm excitation) focused with a 100 ×, NA = 0.9 objective. The spectrometer used a 2400 lines/mm grating. Incident power at the sample was 1 mW, and the integration time was 1 s per spectrum. Raman mapping was performed on the graphene and graphene/hBN overlap areas of the samples before and after SEM treatment using identical settings. For each spectrum, the 2D band was fitted with a Voigt profile to extract peak position and FWHM.

### Twist angle extraction from SEM images

To quantitatively determine the in-plane twist angle induced by electron-beam exposure, we developed a Python routine that performs automated registration between pre- and post-rotation SEM images. The images are converted to 8-bit grayscale and cropped around a fixed region of interest (ROI), typically around 80% of the total field of view, centered on the lithographically defined gold cross deposited on the hBN layer. The algorithm performs a two-stage rigid rotation search: a coarse scan over the interval [-45°, 45°] with 0.05° steps to identify a preliminary minimum, followed by a fine scan within a ± 0.3° window using 0.002° steps. For each trial angle, the post-rotation image is rotated, and the mean squared error (MSE) with respect to the pre-rotation image is calculated over the ROI. The twist angle is defined as the angle that minimizes the MSE, while the uncertainty is estimated as the half-width at which the MSE increases by 1%. The code is provided in Supplementary Data.

## Data availability

Data Availability. All data analysed during this study are available in the Zenodo repository at https://doi.org/10.5281/zenodo.17649829.

## Code availability

The `Rotation_Overlay.py` script for image registration and twist-angle extraction, is available in the Zenodo repository at https://doi.org/10.5281/zenodo.17649829.

Received: 17 September 2025; Accepted: 19 December 2025;
Published online: 31 January 2026

## References

1. Lemme, M. C. et al. Nanoelectromechanical sensors based on suspended 2D materials. *Research* **2020**, 8748602 (2020).
2. Pham, P. V. et al. 2d heterostructures for ubiquitous electronics and optoelectronics: principles, opportunities, and challenges. *Chem. Rev.* **122**, 6514–6613 (2022).
3. Cao, Y. et al. Unconventional superconductivity in magic-angle graphene superlattices. *Nature* **556**, 43–50 (2018).
4. Chiu, M.-H. et al. Spectroscopic signatures for interlayer coupling in MoS2–wse2 van der waals stacking. *ACS Nano* **8**, 9649–9656 (2014).
5. Shi, Z., Wang, X., Sun, Y., Li, Y. & Zhang, L. Interlayer coupling in two-dimensional semiconductor materials. *Semicond. Sci. Technol.* **33**, 093001 (2018).
6. Vargas, A. et al. Tunable and laser-reconfigurable 2d heterocrystals obtained by epitaxial stacking of crystallographically incommensurate Bi2Se3 and MoS2 atomic layers. *Sci. Adv.* **3**, e1601741 (2017).
7. Zhang, C. et al. Interlayer couplings, moiré patterns, and 2d electronic superlattices in MoS2/WSe2 hetero-bilayers. *Sci. Adv.* **3**, e1601459 (2017).
8. Cao, Y. et al. Correlated insulator behaviour at half-filling in magic-angle graphene superlattices. *Nature* **556**, 80–84 (2018).
9. Hanbicki, A. T. et al. Double indirect interlayer exciton in a mose2/wse2 van der waals heterostructure. *ACS Nano* **12**, 4719–4726 (2018).
10. Rivera, P. et al. Observation of long-lived interlayer excitons in monolayer mose2–wse2 heterostructures. *Nat. Commun.* **6**, 6242 (2015).
11. Yankowitz, M. et al. Dynamic band-structure tuning of graphene moiré superlattices with pressure. *Nature* **557**, 404–408 (2018).
12. Ren, W. et al. The 2D Materials Roadmap. 2D Materials (accepted 11 Dec 2025). https://doi.org/10.1088/2053-1583/ae2b82.
13. Ares, P. et al. Piezoelectricity in monolayer hexagonal boron nitride. *Adv. Mater.* **32**, 1905504 (2020).
14. Fan, X. et al. Suspended graphene membranes with attached silicon proof masses as piezoresistive nanoelectromechanical systems accelerometers. *Nano Lett.* **19**, 6788–6799 (2019).
15. Steeneken, P. G., Dolleman, R. J., Davidovikj, D., Alijani, F. & Van der Zant, H. S. Dynamics of 2d material membranes. *2D Mater.* **8**, 042001 (2021).
16. Ryu, Y. K. et al. Microheater actuators as a versatile platform for strain engineering in 2d materials. *Nano Lett.* **20**, 5339–5345 (2020).
17. Gauthier, M. et al. Analysis and specificities of adhesive forces between microscale and nanoscale. *IEEE Trans. Autom. Sci. Eng.* **10**, 562–570 (2013).
18. Dai, Z., Lu, N., Liechti, K. M. & Huang, R. Mechanics at the interfaces of 2d materials: Challenges and opportunities. *Curr. Opin. Solid State Mater. Sci.* **24**, 100837 (2020).
19. Trovatello, C. et al. Optical parametric amplification by monolayer transition metal dichalcogenides. *Nat. Photonics* **15**, 6–10 (2021).
20. Hill, E. H. Layered 2d material heterostructures–a colloidal perspective. *J. Mater. Chem. C.* **12**, 11285–11318 (2024).
21. Vasić, B. et al. Atomic force microscopy based manipulation of graphene using dynamic plowing lithography. *Nanotechnology* **24**, 015303 (2012).
22. Batool, S., Idrees, M., Han, S.-T., Roy, V. A. & Zhou, Y. Electrical contacts with 2d materials: current developments and future prospects. *Small* **19**, 2206550 (2023).

23. Mandelli, D., Leven, I., Hod, O. & Urbakh, M. Sliding friction of graphene/hexagonal–boron nitride heterojunctions: a route to robust superlubricity. *Sci. Rep.* **7**, 10851 (2017).
24. Hennighausen, Z. & Kar, S. Probing the interlayer interaction between dissimilar 2d heterostructures by in situ rearrangement of their interface. *2D Mater.* **6**, 035022 (2019).
25. Woods, C. et al. Macroscopic self-reorientation of interacting two-dimensional crystals. *Nat. Commun.* **7**, 10800 (2016).
26. Eckmann, A. et al. Raman fingerprint of aligned graphene/h-bn superlattices. *Nano Lett.* **13**, 5242–5246 (2013).
27. Kirchhoff, A., Deilmann, T., Krüger, P. & Rohlfing, M. Electronic and optical properties of a hexagonal boron nitride monolayer in its pristine form and with point defects from first principles. *Phys. Rev. B* **106**, 045118 (2022).
28. Cheng, Y. et al. Enhanced p-type conductivity of hexagonal boron nitride by an efficient two-step doping strategy. *Opt. Mater. Express* **14**, 1961–1971 (2024).
29. Ferrari, A. C. & Basko, D. M. Raman spectroscopy as a versatile tool for studying the properties of graphene. *Nat. Nanotechnol.* **8**, 235–246 (2013).
30. Cheng, B. et al. Raman spectroscopy measurement of bilayer graphene's twist angle to boron nitride. *Appl. Phys. Lett*. **107**, 033101 (2015).
31. Finney, N. R. et al. Tunable crystal symmetry in graphene–boron nitride heterostructures with coexisting moiré superlattices. *Nat. Nanotechnol.* **14**, 1029–1034 (2019).
32. Zhu, S., Pochet, P. & Johnson, H. T. Controlling rotation of two-dimensional material flakes. *ACS Nano* **13**, 6925–6931 (2019).
33. Zhang, Z. & Zhu, S. Universal scaling laws on the rotational energy landscape for twisted van der Waals bilayers. *Nanoscale* **17**, 8515–8523 (2025).
34. Halbertal, D. et al. Moiré metrology of energy landscapes in van der Waals heterostructures. *Nat. Commun.* **12**, 242 (2021).
35. Capasso, A. et al. CVD-graphene/graphene flakes dual-films as advanced DSSC counter electrodes. *2D Mater.* **6**, 035007 (2019).
36. Schmuck, O., Beretta, D., Furrer, R., Oswald, J. & Calame, M. A method to fabricate nanoscale gaps in graphene nano-constrictions by electrical breakdown. *AIP Adv*. **12**, 055312 (2022).
37. Petrini, N. et al. Optimizing gold-assisted exfoliation of layered transition metal dichalcogenides with (3-aminopropyl) triethoxysilane (aptes): A promising approach for large-area monolayers. *Adv. Opt. Mater.* **12**, 2303228 (2024).
38. Petrini, N., Asaithambi, A., Rebecchi, L. & Curreli, N. Bismuth telluride iodide monolayer flakes with nonlinear optical response obtained via gold-assisted mechanical exfoliation. *Opt. Mater.: X* **19**, 100255 (2023).
39. Sunku, S. S. et al. Dual-gated graphene devices for near-field nano-imaging. *Nano Lett.* **21**, 1688–1693 (2021).


## Acknowledgements

N.C. acknowledges support from the European Union's Horizon Europe research and innovation programme through the Marie Skłodowska-Curie Actions under grant agreement No. 101109662 (2DTWIST). R.S. and M.C. acknowledge funding from the European Union's Horizon Europe research and innovation programme under grant agreement number 101099098 (ATYPIQUAL). N.P. and I.K. acknowledge financial support from the European Union's Horizon 2020 research and innovation programme through the European Research Council (ERC) under grantagreement No. 850875 (Light-DYNAMO project), and from the European Union under grant agreement No. 101186701 (LEAF project). The authors thank the Electron Microscopy Facility and the Material Characterization Facility of the Italian Institute of Technology for support with material characterization, as well as the support provided by the Clean Room Facility of the Italian Institute of Technology and the staff of the Binnig and Rohrer Nanotechnology Center (BRNC) for device fabrication.

## Author contributions

N.C. conceived and designed the experiments, performed the experiments, analyzed the data, contributed analysis tools, and wrote the manuscript. T.S.K., R.S., N.P., M.B.L., R.F., and A.F. contributed to experiments and data analysis. M.C. and I.K. contributed to the conception of the experiments and supervised the project. All authors reviewed and approved the manuscript.

## Competing interests

The authors declare no competing interests.

## Additional information

**Supplementary information** The online version contains supplementary material available at https://doi.org/10.1038/s41699-025-00658-x.

**Correspondence** and requests for materials should be addressed to Nicola Curreli.

**Reprints and permissions information** is available at http://www.nature.com/reprints

**Publisher's note** Springer Nature remains neutral with regard to jurisdictional claims in published maps and institutional affiliations.

**Open Access** This article is licensed under a Creative Commons Attribution 4.0 International License, which permits use, sharing, adaptation, distribution and reproduction in any medium or format, as long as you give appropriate credit to the original author(s) and the source, provide a link to the Creative Commons licence, and indicate if changes were made. The images or other third party material in this article are included in the article's Creative Commons licence, unless indicated otherwise in a credit line to the material. If material is not included in the article's Creative Commons licence and your intended use is not permitted by statutory regulation or exceeds the permitted use, you will need to obtain permission directly from the copyright holder. To view a copy of this licence, visit http://creativecommons.org/licenses/by/4.0/.

© The Author(s) 2026